Transmission electron microscopy of dislocations in cementite deformed at high pressure and high temperature

Alexandre Mussi, Patrick Cordier, Sujoy Ghosh, N. Garvik, Billy Clitton Nzogang, Philippe Carrez, S. Garruchet

Philosophical Magazine

ISSN: 1478-6435 (Print) 1478-6443 (Online) Journal homepage: http://www.tandfonline.com/loi/tphm20

Transmission electron microscopy of dislocations in cementite deformed at high pressure and high temperature

A. Mussi, P. Cordier, S. Ghosh, N. Garvik, B. C. Nzogang, Ph. Carrez & S. Garruchet

To cite this article: A. Mussi, P. Cordier, S. Ghosh, N. Garvik, B. C. Nzogang, Ph. Carrez & S. Garruchet (2016): Transmission electron microscopy of dislocations in cementite deformed at high pressure and high temperature, Philosophical Magazine, DOI: 10.1080/14786435.2016.1177670

To link to this article: http://dx.doi.org/10.1080/14786435.2016.1177670

Published online: 05 May 2016.

PHILOSOPHICAL MAGAZINE, 2016
http://dx.doi.org/10.1080/14786435.2016.1177670

Taylor & Francis
Taylor & Francis Group

Transmission electron microscopy of dislocations in cementite deformed at high pressure and high temperature

A. Mussi[a], P. Cordier[a], S. Ghosh[b,c], N. Garvik[a], B. C. Nzogang[a], Ph. Carrez[a] and S. Garruchet[d]

[a]Unité Matériaux et Transformations, UMR-CNRS 8207, Université Lille1, Sciences et Technologies, Villeneuve d'Ascq, France; [b]Institut für Geochemie und Petrologie, ETH, Zürich, Switzerland; [c]Department of Geology and Geophysics, IIT Khargapur, Khargapur, India; [d]Manufacture Française des Pneumatiques MICHELIN, Centre de Ladoux, Clermont-Ferrand, France

ABSTRACT

Polycrystalline aggregates of cementite (Fe_3C) and $(Fe,Ni)_3C$ have been synthesised at 10 GPa and 1250 °C in the multianvil apparatus. Further, deformation of the carbides by stress relaxation has been carried out at temperature of 1250 °C and for 8 h at the same pressure. Dislocations have been characterised by transmission electron microscopy. They are of the [1 0 0] and [0 0 1] type, [1 0 0] being the most frequent. [1 0 0] dislocations are dissociated and glide in the (0 1 0) plane. [0 0 1] dislocations glide in (1 0 0) and (0 1 0). Given the plastic anisotropy of cementite, the morphology of the lamellae in pearlitic steels appears to have a major role in the strengthening role played by this phase, since activation of easy slip systems is geometrically inhibited in most cases.

ARTICLE HISTORY
Received 30 January 2016
Accepted 7 April 2016

KEYWORDS
Cementite; dislocations; plastic deformation; transmission electron microscopy

1. Introduction

Cementite Fe_3C is the main iron carbide in pearlitic steels and plays a pivotal role in determining their strength. Cementite exhibits an orthorhombic symmetry. When described within the space group *Pnma*,[1] lattice parameters are $a = 5.03$ Å, $b = 6.71$ Å and $c = 4.53$ Å. A Fe_3C unit cell contains 12 iron atoms and 4 carbon atoms. Regarding mechanical stability, this material is strongly anisotropic in terms of elasticity and ultimate properties [4,13]. Despite numerous studies on the mechanical properties of these alloys, our understanding on the basic deformation mechanisms of cementite is still incomplete. Several evidence have been provided that cementite can exhibit a ductile behaviour [3,10,11,15,17,27,28]. Very few microstructural investigations have been carried out to characterise elementary deformation mechanisms in cementite, including dislocations and slip systems. Most Burgers vectors which are likely to exist in this orthorhombic structure (i.e. [1 0 0], [0 1 0] and [0 0 1]) have been proposed [10,11,17,27], but detailed characterisations are scarce. In a recent study, Kar'kina et al. [14] have drawn attention on the contribution of partial [1 0 0] dislocations gliding in (0 1 0) in cold plastic deformation of cementite in granular pearlite.

CONTACT P. Cordier Patrick.Cordier@univ-lille1.fr

It has long been recognised that cementite becomes more stable under increasing pressure [31]. Recently, Rohrbach et al. [26] have shown that coarse-grained cementite could be synthesised from multianvil experiments. They observed that eutectic temperature of Fe–Ni–C system is very low (1125 °C at an X_{Ni} of 0.5) compared to Fe–C system (i.e. 1210 °C at the Fe–C side) in the reduced phase.

In this study, cementite has been synthesised at high pressure and temperature in the multianvil apparatus and subsequently deformed in an experiment slightly modified to apply deviatoric stresses. The dislocations are characterised by transmission electron microscopy (TEM).

2. Methods

2.1. Starting materials

Two different starting materials are used in the present study. In the Fe–C system, starting material is on the pure Fe_3C composition which is a mixture of pure powder of Fe (99.9% purity powder from 'Alfa Aesar') and mono crystalline diamond (1/4–3/4 μm grain size from 'Microdiamant') in $Fe_{92.5}C_{7.5}$ composition (in wt.%) and another composition is a mixture of pure powders of Fe and Ni (99.9% purity powder from 'Alfa Aesar') with diamond powder in $Fe_{82.5}Ni_{10}C_{7.5}$ (in wt.%). Previous experiments [26] have shown that using graphite should be avoided because it makes reaction kinetics very slow and experimental charge does not reach equilibrium in few hours. Also graphite is very light and segregates in flakes during mixing under ethanol in the agate mortar and creates slightly compositional heterogeneities. All ingredients were stored in a sensor-controlled desiccator to avoid their hydration or oxidation. The powders were stored in a drying furnace at 110 °C until used. In general, starting mixes were prepared shortly prior to experimentation to avoid oxidation.

2.2. Multianvil experiments

Experiments were carried out in 1000-ton Walker-type multianvil devices at 10 GPa and 1250 °C at the Institute of Geochemistry and Petrology, ETH Zürich. We used 18/11 assemblies with chromium-doped MgO octahedra, stepped $LaCrO_3$ furnaces and pyrophyllite gaskets. Details of assembly design and pressure calibration of the Zurich multianvil are given in Grassi and Schmidt [6].

For the synthesis of carbides used in this study, the starting powder was encapsulated into polycrystalline crushable Al_2O_3 containers (porosity 30%), two of which were stacked upside down into the centre part of the furnace. Run temperature was measured with type C thermocouples and no pressure correction on the *emf* was applied. Experiments were brought up to 10 GPa, heated to the 1250 °C at a rate of ~50°/min and annealing for 30 h at the same pressure (synthesis run # DFC-1). The combined uncertainty of the temperature measurement, which results from temperature fluctuations during the run (±5 °C) and temperature gradients within the assembly, is estimated to be about ±20 °C. Samples were quenched by turning off the power supply, resulting in reducing the temperature to below 500 °C in <1 s. After the first run of synthesis, the resulting cementite [Fe_3C and $(Fe,Ni)_3C$] phases were extracted from the compressed high-pressure cell. They were then positioned in another high-pressure cell designed to induce deviatoric stresses by adding

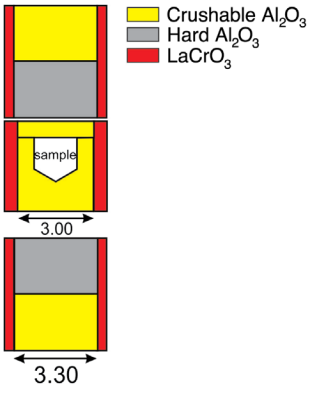

Figure 1. (colour online) Schematic cross section of cell assembly used for the present deformation experiments with the 18/11 assembly (unit: mm).

hard alumina pistons [2]. Deformation experiments were conducted at the same pressure and at temperatures of 1250 °C than synthesis, for 8 h (deformation run # DFC-2 is Ni-free and deformation run # DFC-3 is with Ni). A diagram of the cell assembly for deformation experiment is given in Figure 1.

2.3. Transmission electron microscopy

The samples have been mechanically polished down to *ca.* 30 µm thick. The resulting foils were ion sputtered with a Gatan® DuoMill TM model 600, to reach electron transparency. TEM characterisations were performed at the TEM facility at the University of Lille1, with a FEI® Tecnaï $G^2$20Twin microscope, operating at 200 kV and a FEI® CM30 microscope, operating at 300 kV, both equipped with a LaB_6 filament. Dislocation microstructures were investigated in the weak-beam dark-field (WBDF) mode. Energy-filtered WBDF images were acquired (in order to keep the elastic electrons only) to distinguish fine dislocation details, using a Gatan® imaging filtering model 2000 electron energy loss spectrometer coupled to the microscope [21]. Precession electron diffraction (PED) was performed using a 'Spinning Star' precession module from the NanoMEGAS' Company. In PED technique, the incident beam is scanned at a constant precession angle (ranging from 1° to 3°) around the optical axis, in combination with an opposite and synchronised descan of the transmitted and diffracted beams below the specimen [29]. During the precession movement, the reciprocal lattice nodes are thus swept through the Ewald sphere and integrated intensities over a large range of deviation parameter *s* around the Bragg orientation are collected. PED has the following main advantages: (1) the zone axis patterns are very symmetrical, even if the specimen zone axis is not exactly located along the optical axis; (2) the incident beam is never directed along the zone axis so that dynamical interactions are strongly reduced; (3) with large precession angles, a 'two-beam' behaviour is observed, which limits the multiple diffraction paths and allows the identification of the kinematical forbidden reflections; and (4) very small differences of intensity are visible. Hence, diffraction patterns carry not only geometrical information, but also intensity information which enhances reliability in pattern indexation. Electron diffraction pattern were simulated using the 'Electron

Diffraction' software from Morniroli et al. [19]. TEM-based orientation mapping [23,24] has been performed using the NanoMEGAS' ASTAR/DigiSTAR precession-assisted crystal orientation mapping technique. Electron diffraction spot patterns were collected sequentially with a 20 nm step size (typical mapped areas are of the order of 5 μm × 5 μm) using the microprobe mode with a beam diameter of 30 nm and a condenser aperture of 10 μm. The beam was precessed (precession angle 0.6°) around the optical axis of the microscope to reduce strong dynamical effects and increase the number of reflections. Once the automated acquisition of several thousands of precessed diffraction patterns has been completed, orientation identification is performed for each individual pattern, via comparison with previously generated model templates. For each individual experimental diffraction pattern, a specific best orientation is automatically chosen with an associated degree of confidence in the choice; this is called the reliability and maps can be issued featuring this parameter. Reliability maps clearly reveal grain and phase boundaries. Transmitted beam intensity fluctuation maps (called virtual bright field images) can be produced by integrating the intensity within a virtual aperture placed on the same position for all diffraction patterns.

Electron tomography was performed with a double-tilt sample holder with a maximal angular range of ±60°. As in our previous work [20], the obtained tilted series have been manually centred within one pixel accuracy, and then filtered with the ImageJ software to enhance the dislocation contrast, and improve the background and dislocation contrast homogeneity. The 3D images have been generated with two reconstruction algorithms: The simultaneous iterative reconstruction technique algorithm [22] used with the Gatan® 3D reconstruction software; and the weighted back projection algorithm [7] used with the TomoJ plugin [18] accessible in ImageJ.

In the LACBED configuration, the specimen is not located in the object plane, i.e. at the focused beam crossover, as in the conventional CBED mode. A selected-area aperture (10 μm in diameter) is introduced in the image plane to select the transmitted beam to form a bright field LACBED pattern. Such patterns display many Bragg lines coming from various layers of the reciprocal space superimposed to a shadow image of the illuminated area of the specimen. The small size of the selected area aperture has been used to obtain filtered LACBED patterns (thin Bragg lines can be distinguished). In LACBED, the ***g.b*** product is obtained by counting the nodes of a split Bragg line crossing a dislocation line [1]. Interactions with three independent Bragg lines allow unambiguous determination of the Burgers vector without any assumption.

3. Results

Both samples appear to be very similar showing that the Ni content does not affect significantly the deformation mechanisms activated. The samples are coarse-grains polycrystals with cementite grain sizes ranging from one micrometre to a few tens of micrometres (see Figure 2) which form a load-bearing structure. Some secondary phases (they appear in black in Figure 2 since they are not indexed with the cementite structure) can be observed at grain boundaries or sometimes inside the cementite grains. Several grains exhibit dislocation activity, but not all. On all grains in which dislocations have been characterised, zone axis patterns have been acquired in PED to check for the cementite crystal structure, to orientate the grain and to select diffraction vectors with large structure factors (Table 1)

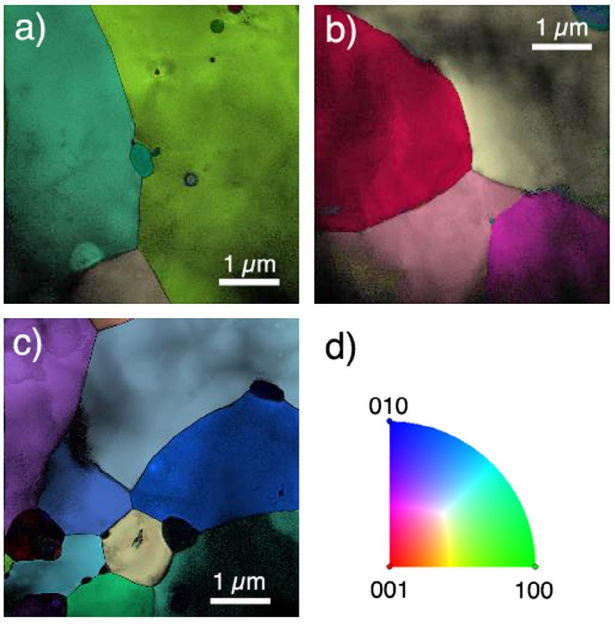

Figure 2. (colour online) Orientation maps (a–d). Each figure is a combination of the orientation map, of the virtual bright field and of the reliability. (a) Orientation map along *z*. (b–c) Orientation maps along *y*. (d) Colour code.

Table 1. Intensity (and d_{hkl}) of the most intense reflections in Fe_3C cementite (calculated with electron diffraction).

{h k l}	d_{hkl} (Å)	Intensity
0 0 2	2.2615	636
2 1 1	2.1071	563
1 0 2	2.0667	933
2 2 0	2.0318	1065
0 3 1	2.0140	2090
1 1 2	1.9761	677
2 2 1	1.8534	663
2 3 0	1.6854	534
3 0 1	1.5886	577
4 0 1	1.2249	721
3 3 2	1.1620	524
3 0 3	1.1270	740
0 6 0	1.1247	956
4 3 0	1.1076	715

in order to perform observations in WBDF. Figure 3 presents an example of electron diffraction characterisation of a cementite grain on which dislocations have been characterised.

Figure 4 shows a typical microstructure observed in sample DFC-2. Two families of dislocations are present. On Figure 4(a), imaged with *g*: 0 0 2, only [0 0 1] dislocations are in contrast (Δ and Δ′). Residual contrasts suggest the presence of other dislocations. They are probably due to some edge components (A and B) or sometimes just to the elastic relaxation where the dislocation lines meet the free surfaces of the thin foil (see for instance dislocations C and D). Indeed, when the same area is imaged with *g*: -211, another population of dislocations appears. In the thinnest part of the micrographs, thickness fringes

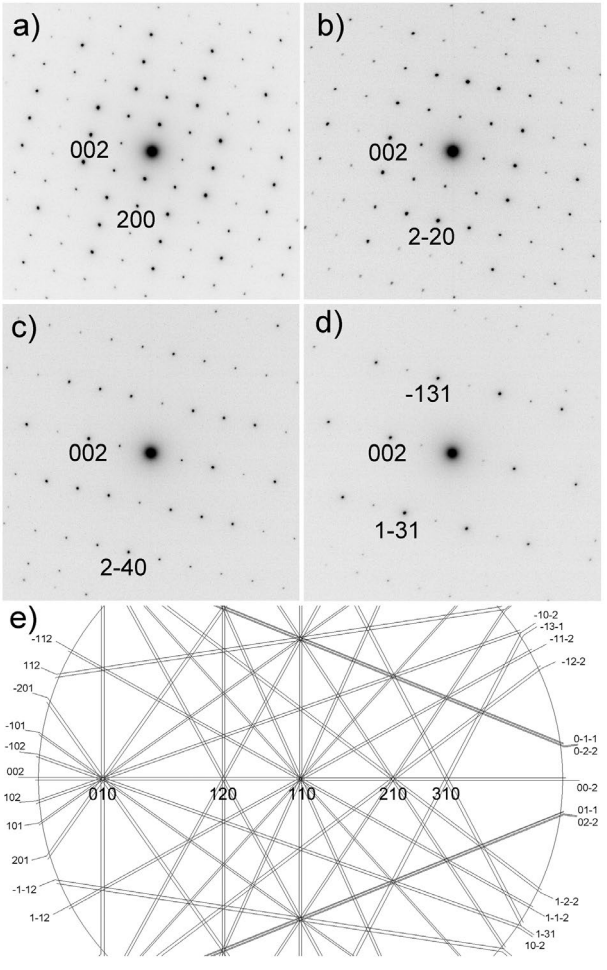

Figure 3. Sample DFC-3 – PED (precession angle 2°) on the grain imaged on Figures 4 and 5. (a) [0 1 0] zone axis pattern. (b) [1 1 0] zone axis pattern. (c) [2 1 0] zone axis pattern. (d) [3 1 0] zone axis pattern. (e) Kikuchi map figuring the orientation sampled.

can be used to further constraint the Burgers vectors following the technique proposed by Ishida et al. [12]. Dislocations E and F clearly show that two thickness fringes terminate on the dislocations lines which are characteristic of a ***g.b*** product equal to 2. Hence, those dislocations are of the [1 0 0] type. Very similar microstructures are found in the other sample (DFC-3) as illustrated on Figure 5. Only [1 0 0] dislocations (labelled a, b, c, d, e, f and g) are in contrast in Figure 5(a) with *g*: -220 , whereas both [1 0 0] and [0 0 1] dislocations (the latter labelled with Greek letters) are visible on Figure 5(b). One can check that one thickness fringe terminates on [0 0 1] dislocations imaged with *g*: -22-1 (see α and β for instance), whereas two fringes terminate on [1 0 0] dislocations (see for instance a, b or c).

In any case, we couldn't find any significant evidence for [0 1 0] dislocation activity. Figure 6 shows a micrograph where a grain was oriented to select a *g*: 0 6 0 diffraction vector to image the microstructure. This reflection which has a high structure factor (Table 1) should clearly reveal the presence of [0 1 0] dislocations. Such is not the case. Figure 6 shows that we can

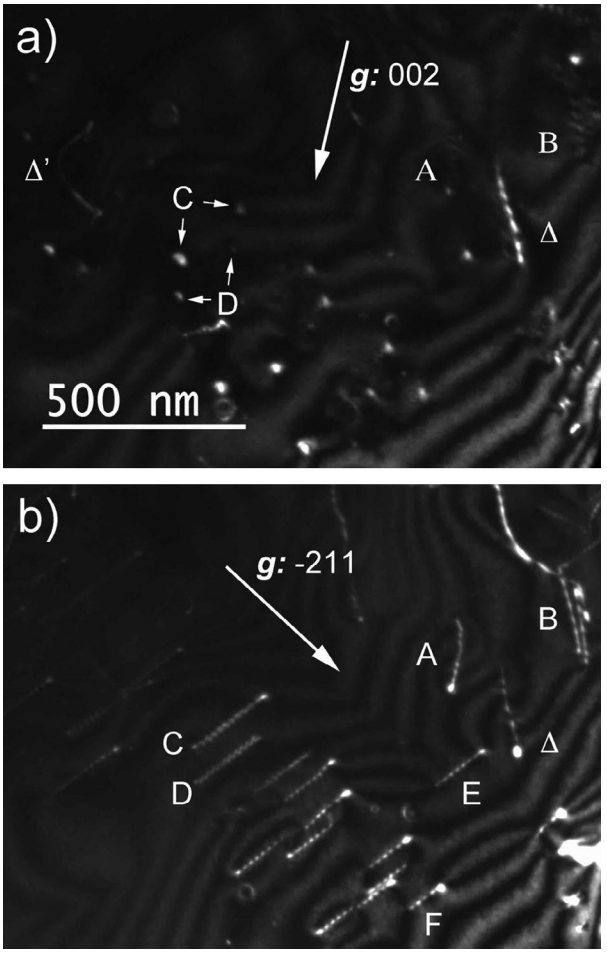

Figure 4. Sample DFC-2 – WBDF micrographs performed with: (a) g_1: 002 close to the [1 2 0] zone axis. (b) Same area as (a) and same magnification. g_2: -211 close to the [1 2 0] zone axis.

only see residual contrast of dislocations out of contrast. To further establish the dislocation types present in the sample, we have carried out LACBED characterisations which provide robust determination of Burgers vectors without any a priori hypothesis. Only [1 0 0] and [0 0 1] dislocations have been identified (see Figures 7 and 8).

The glide planes of dislocations can be identified by tilting the specimen until the planes are edge-on. A curved dislocation appears as a straight segment under this orientation. An example is shown in Figure 9 where a [0 0 1] dislocation line with a clear bent appears straight when its glide plane, (1 0 0) is seen edge-on. The difficulty with this technique is that the useful orientation may not be reached within the tilt range of the specimen holder. Electron tomography is a way to overcome this limitation. Figure 10 presents such a case where a long [0 0 1] segment with a small but detectable curvature could not be put edge-on experimentally. However, after having recorded a tilt series and performed a tomographic reconstruction, we could show that this dislocation is gliding in the (0 1 0) plane.

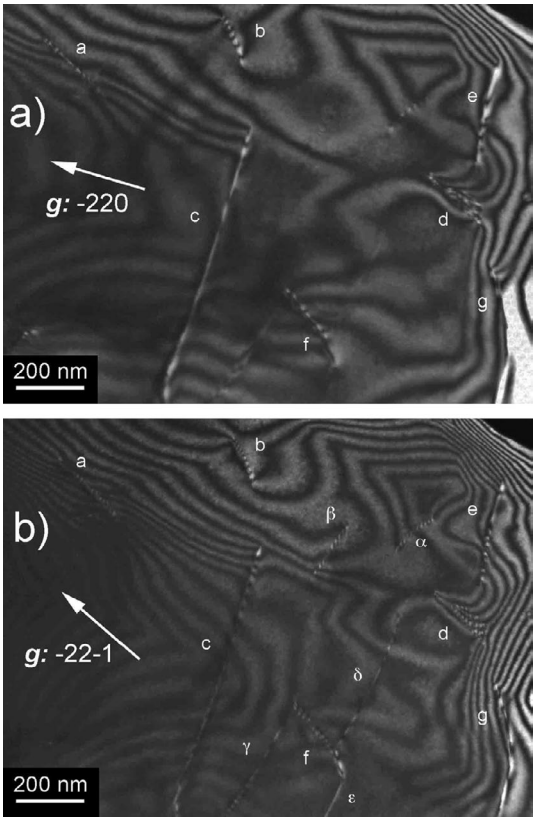

Figure 5. Sample DFC-3 – WBDF micrographs performed with: (a) g_1: -220 close to the [1 1 0] zone axis. (b) same area as (a). g_2: -22-1 close to the [1 1 0] zone axis.

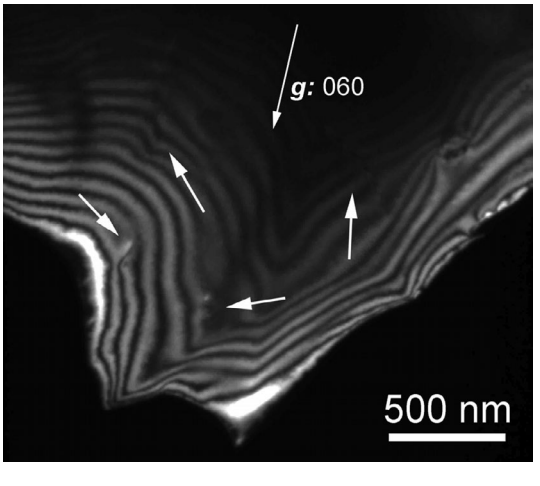

Figure 6. Sample DFC-2 – WBDF micrographs performed with: *g*: 0 6 0 to look for possible evidences of [0 1 0] dislocations. No dislocation is found in contrast with *g*: 0 6 0 in any area investigated. The contrasts arrowed here are only residual contrasts related to [0 0 1] dislocations.

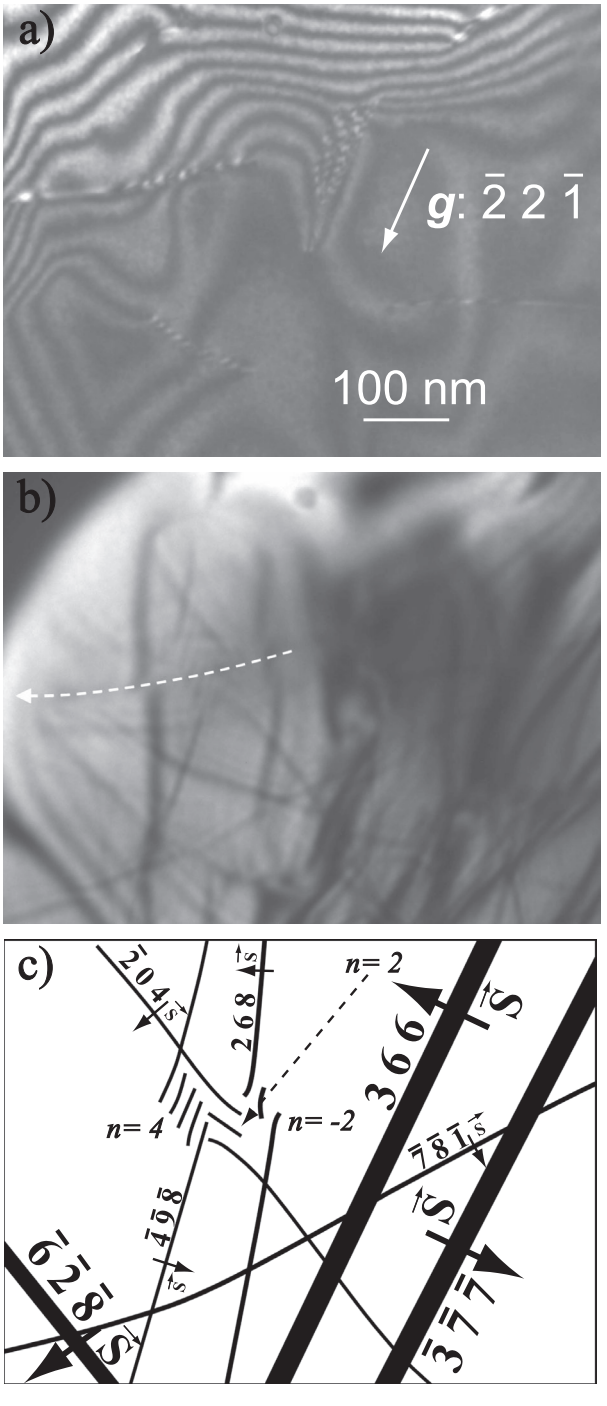

Figure 7. Sample DFC-3 – Indexation of a [1 0 0] dislocation using the LACBED technique. (a) WBDF image with g: -22-1 showing the dislocation studied. (b) Experimental LACBED pattern crossing a dislocation (dotted arrow). The splittings of the Bragg lines can clearly be observed. (c) From the three identified splitting (with the -4-9-8, -204, 268 Bragg lines) the Burgers vector $[\bar{1}\,0\,0]$ can be identified. Additional effects (not shown) with the -3-3-8, -4-6-1 Bragg lines have also been observed for this dislocation.

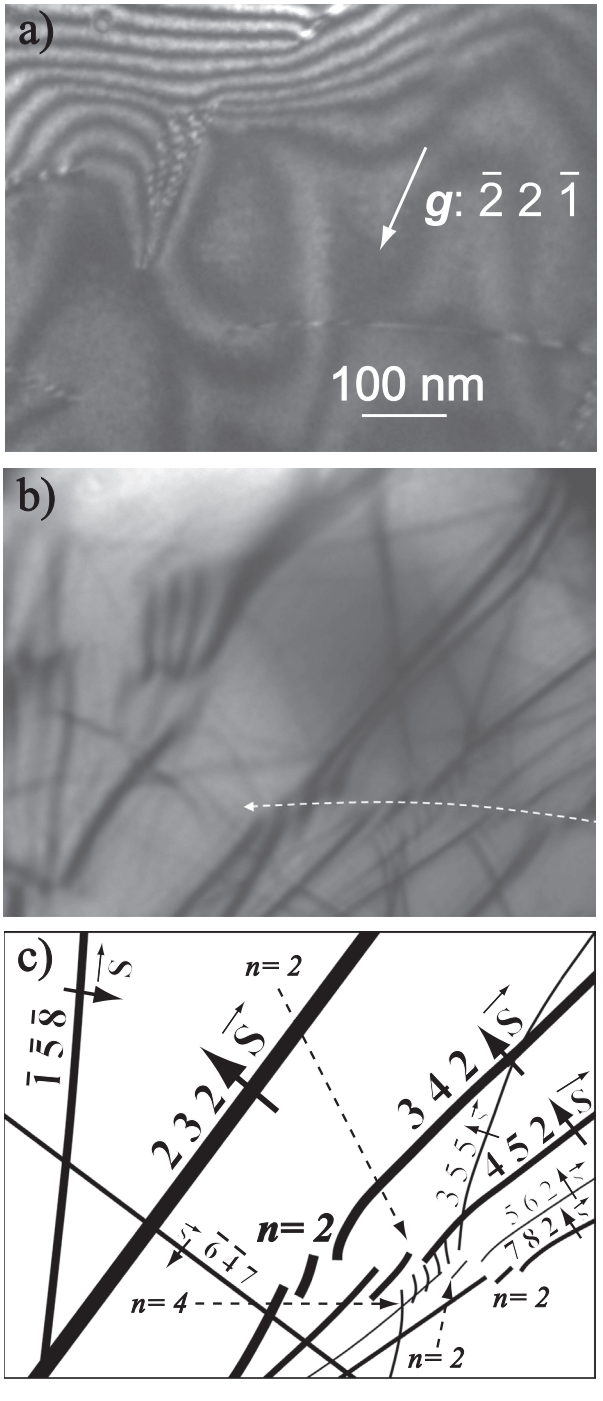

Figure 8. Sample DFC-3 – Indexation of a [0 0 1] dislocation using the LACBED technique. (a) WBDF image with g: -22-1 showing the dislocation studied. (b) Experimental LACBED pattern. (c) Burgers vector determination resulting from the crossings with the 3 4 2, 4 5 2, 3 5 5, 5 6 2, 7 8 2 Bragg lines). The Burgers vector [0 0 1] is identified.

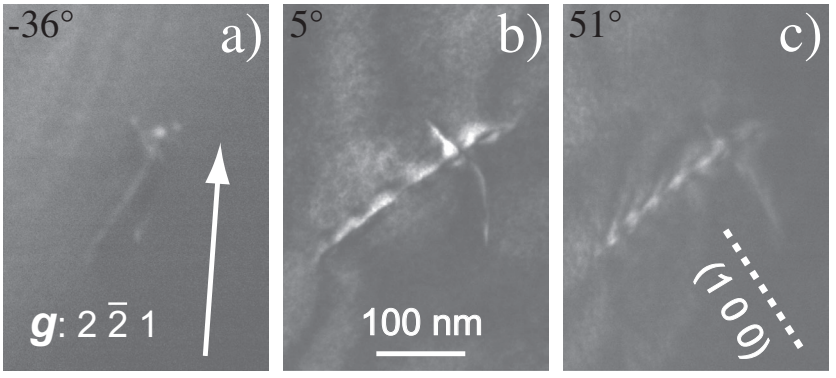

Figure 9. Sample DFC-3 – [0 0 1] dislocation gliding in (1 0 0). (a) WBDF image with g: 2-21, obtained with the −36° tilt angle. The micrograph shows a straight [1 0 0] dislocation line and a highly curved [0 0 1] dislocation. (b) WBDF micrograph in the same diffraction condition as (a), projected with a tilt angle of 5°. The [0 0 1] dislocation is less curved than in (a). (c) WBDF image obtained with the same diffraction vector as (a) and (b), with a projected angle of 51°. The [0 0 1] dislocation appears as a straight line since its glide plane is edge-one. This plane corresponds to (1 0 0).

The case of [1 0 0] dislocations is more interesting. There are many evidences that these dislocations exhibit a double contrast which suggests a dissociation. Figure 11(a) displays such a case. Imaged in WBDF with *g*: 2-20, this dislocation clearly exhibits a contrast made of two lines of equivalent intensity. The same dislocation imaged with *g*: 1 0 2 reveals the characteristic contrast of the stacking fault ribbon located between these two partial dislocations (see Figure 11(b)). This contrast is thus compatible with a dissociation following the reaction $[1\,0\,0] = \frac{1}{2}[1\,0\,0] + \frac{1}{2}[1\,0\,0]$. The dissociation plane is of major interest since it is the plane where this dislocation will be able to glide. To characterise this plane, we have again used electron tomography to find that the dissociation plane is (0 1 0) (see Figure 12). Indeed, we can verify that the glide plane of the second dissociated [1 0 0] dislocation, on the lower part of the micrographs in Figure 12, coincides with the dissociation plane. From this characterisation, it is also possible to deduce the dissociation width: 12 nm.

Finally, must also be noted that only few evidence where found for dislocation reactions (junctions) or for subgrain formation.

4. Discussion and conclusion

Our study shows that at 1250 °C, cementite can be plastically deformed by dislocation glide as already suggested by the early studies of Keh [15], Koréeda and Shimizu [17], Sevillano [27] and Inoue et al. [8,9]. Inoue et al. [10,11] attempted to determine the Burgers vector of dislocations in deformed cementite. They found mostly [1 0 0] dislocations. More recently, Kar'kina et al. [14] showed that, at the early stages of deformation of granular pearlite, carbide particles are deformed by partial [1 0 0] dislocations. Our study does confirm the importance of [1 0 0] glide in the plasticity of cementite. Although statistics is always a difficult issue in TEM observations, it remains a fact that most of the dislocations that we observed are of the [1 0 0] type. Another interesting observation is that [1 0 0] dislocations are dissociated. In a recent study, we used the Peierls Nabarro model to determine the core structure of [1 0 0] dislocations (Garvik et al. [5]). We showed that they exhibit core

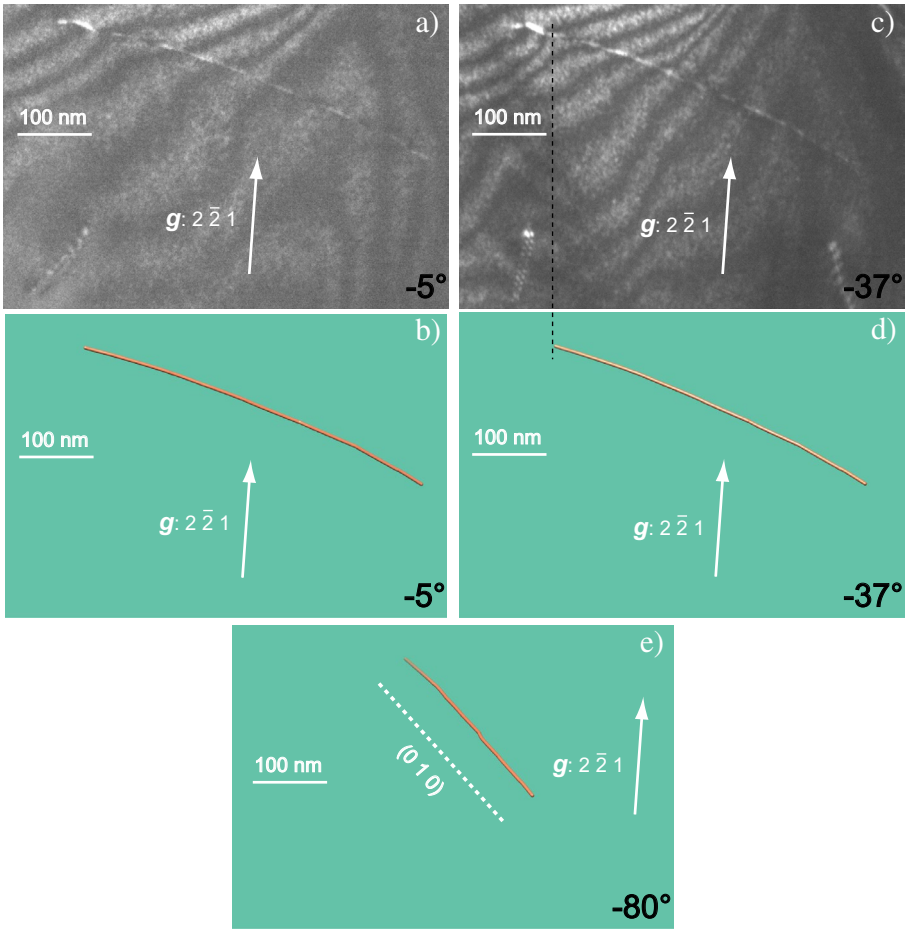

Figure 10. (colour online) Sample DFC-3 – [0 0 1] dislocation gliding in (0 1 0). (a) WBDF micrograph obtained with g: 2-21, tilt angle: –5°. (b) Corresponding reconstruction volume. (c) WBDF micrograph in the same diffraction conditions as (a), tilt angle: –37°. The [0 0 1] dislocation seems to have interacted with a small [0 0 1] dislocation loop. A black dashed line helps to distinguish the long [0 0 1] dislocation from the small loop. (d) Corresponding volume without the dislocation loop. (e) Reconstructed volume (tilt angle: –80°). The dislocation glide plane is edge-on and its trace corresponds to (0 1 0).

spreading in the (0 1 0) plane. We confirm here that [1 0 0] dislocations are dissociated in this plane. At high temperature, the dissociated dislocations glide at once (i.e. with partial dislocations still correlated) in the (0 1 0) plane. However, the Peierls Nabarro model suggests two asymmetric partials which may experience different lattice frictions (Garvik et al. [5]). At lower temperature and under high stress, the two partials may de-correlate leading to a deformation by partials as observed by Kar'kina et al. [14] (also probably reported by Keh [15] although some ambiguity remain on the plane containing the stacking fault reported in their work where the space group used is not precised).

The second occurrence of dislocations corresponds to a [0 0 1] Burgers vector. Evidence for [0 0 1] glide are dubious in the literature, but their occurrence has been suggested in subgrain boundaries by Inoue et al. [10,11]. In our study, these dislocations appeared not to be dissociated in agreement with our core modelling [5]. They glide in (1 0 0) and (0 1 0).

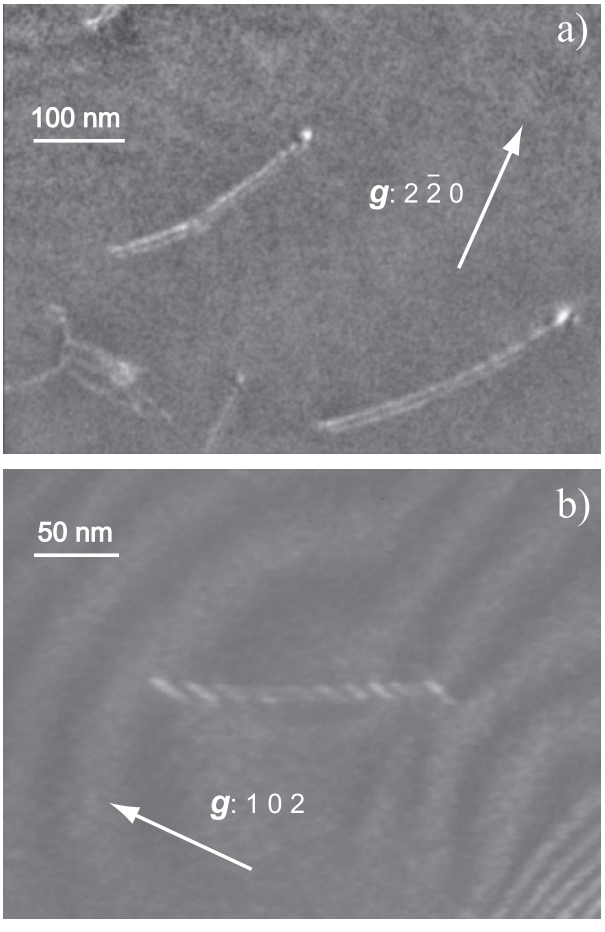

Figure 11. Sample DFC-3 – Dissociated [1 0 0] dislocations. (a) Energy filtered WBDF micrographs with g: 2-20 (g.b = 1 with b = ½[1 0 0]); and beam precessed with an angle of 0.25° to remove the dislocation oscillating contrast and the thickness fringes contrast [20,25]. The two ½[1 0 0] partial dislocations can clearly be seen. (b) WBDF micrograph with g: 1 0 2 (g.b = ½ with b = ½[1 0 0]). The stacking fault is in contrast while the partial dislocations are out of contrast with this diffraction condition.

Finally, we could not find any significance evidence for [0 1 0] glide. Here again, comparison with the literature is uncertain, however, to the best of our knowledge, we could not find any clear evidence for such dislocations.

From the kinematic point of view, the ductility of a polycrystalline aggregate is linked to the availability of five independent slip systems. In cementite this is clearly questionable. Following Kim et al. [16], Umemoto et al. [28] showed that above 773 K, bulk cementite polycrystals could be plastically deformed under the operation of grain boundary processes due to small grain sizes. The ductility of large grain aggregates through intracrystalline mechanisms still remains an open issue. The situation is slightly different in pearlitic steels where cementite exhibits a lamellar morphology embedded in a ferritic matrix. Strain incompatibilities at the ferrite/cementite interface are certainly a key issue in understanding the ability of cementite to deform, but morphology may be important as well. Again there are ample evidence that cementite lamellae undergo plastic deformation. For instance,

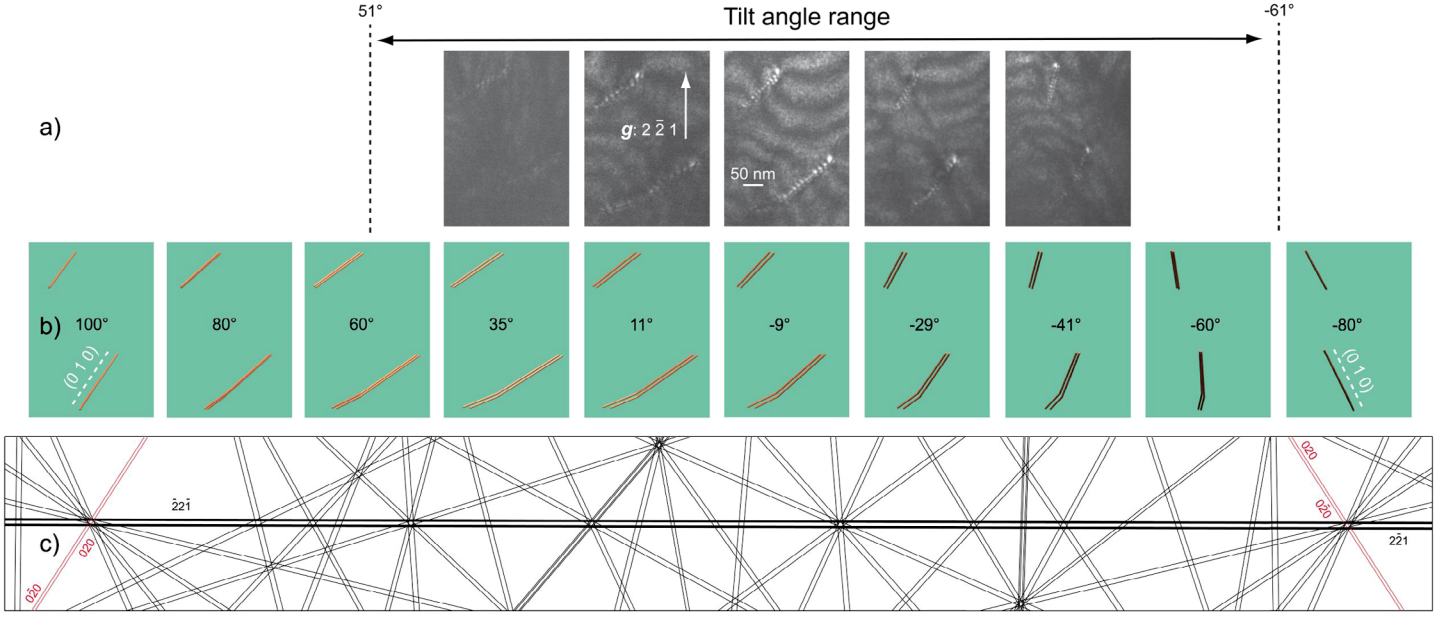

Figure 12. (colour online) Sample DFC-3 – Glide and dissociation plane of [1 0 0] dislocations. (a) experimental WBDF micrographs obtained using the 2-21 diffraction vector. The tilt angles are, respectively, 35°, 11°, −9°, −29° and −41°. The black arrow indicates the tilt angle range experimentally available in the microscope (between −61° and 51°). (b) 3D reconstruction volume projected along the directions as in (a) and also projected within the missing wedge (tilt angles are reported on the figures). The glide and dissociation planes of the [1 0 0] dislocations are edge-on along −80° and 100°. (c) Simulation of the Kikuchi lines (in kinematics conditions), between −80° and 100°, obtained with the Electron Diffraction software [19]. The orientations of the Kikuchi lines of (0 1 0) correspond to the glide and dissociation plane trace of the [1 0 0] dislocations along −80° and 100° in (b) (red lines).

Umemoto et al. [28] showed evidence for striction, buckling and more importantly of slip traces on cementite lamellae demonstrating single slip activity. Unfortunately, the crystallographic orientation of the lamellae was not provided in Umemoto et al. [28]. The nature of crystallographic relationships between ferrite and cementite has been revisited by Zhang et al. [30] who suggest a few low-misfit habit planes. Among them, (0 1 0) would correspond to the smallest interfacial energy barrier and to the smallest transformation strain. This morphology has been observed by Fang et al. [3] who report dislocation activity transmitted into cementite lamellae across the (0 1 0) interface (personal communication on the use of the *Pbnm* space group in their publication). The two Burgers vectors for easy glide being parallel to this habit plane, any shear would need to activate hard [0 1 0] glide in a direction perpendicular to the lamellae habit plane, contributing to a hard response of cementite. This scenario is compatible with the observation reported by Umemoto et al. [28] in their Figure 1. The two other habit plane proposed by Zhang et al. [30] are (1 3 0) and (1 1 0). The occurrence of lamellae along (1 3 0) would lead to the same behaviour with [0 0 1] parallel to the lamellae and [1 0 0] lying at only 14° from the interface. Only (1 1 0) would lead to a slightly softer situation with one easy slip direction, [1 0 0] oriented at 53° from the normal of the lamellae. Still only one easy slip system would be available.

5. Conclusion

Our study highlights the importance of [1 0 0] and [0 0 1] slip in the plasticity of cementite. We observe that [1 0 0] dislocations are dissociated in agreement with our theoretical prediction (Garvik et al. [5]) and with the observation of activation of partial [1 0 0](0 1 0) dislocations in cementite deformed at low temperature (Keh [15] and Karkina et al. [14]). The strengthening role played by cementite in pearlitic steels would thus also be controlled by the morphology. Considering the observation of lamellae parallel to (0 1 0) reported by Fang et al. [3], one notes that transmission of plasticity into the cementite phase can only be activated along one direction [0 1 0] which seems to be the most difficult to activate. Only lamellae parallel to (1 1 0), as proposed by Zhang et al. [30], would allow to activate easy [1 0 0] slip. Given the plastic anisotropy of cementite, the morphology of the lamellae in pearlitic steels appears to have a major role in the strengthening role played by this phase.

Note

1. All planes and directions indicated in this publication are described within the *Pnma* space group. When referring to a publication using a different convention, the indices have been permuted.

Acknowledgement

The authors thank two anonymous reviewers which led us to improve our manuscript.

Disclosure statement

No potential conflict of interest was reported by the authors.

Funding

The TEM facility in Lille (France) was supported by the Conseil Regional du Nord-Pas de Calais; the European Regional Development Fund (ERDF). At ETH Zürich, S.G. was supported by a SNF grant [grant number 200020-130100/1].

ORCID

A. Mussi http://orcid.org/0000-0003-2093-0144
P. Cordier http://orcid.org/0000-0002-1883-2994

References

[1] D. Cherns and A.R. Preston, *CBED Studies of Crystal Defect*, Proceedings of the 11th International Congress on Electron Microscopy Vol. 1, Kyoto, 1986, T. Imura, S. Marusa, and T. Suzuki, eds., Japan Society of Electron Microscopy, 1986, pp. 721–722.
[2] P. Cordier and D. Rubie, *Plastic deformation of minerals under extreme pressure using a multi-anvil apparatus*, Mater. Sci. Eng., A 309–310 (2001), pp. 38–43.
[3] F. Fang, Y. Zhao, P. Liu, L. Zhou, X.-j. Hu, X. Zhou, and Z.-h. Xie, *Deformation of cementite in cold drawn pearlitic steel wire*, Mater. Sci. Eng., A 608 (2014), pp. 11–15.
[4] N. Garvik, P. Carrez, and P. Cordier, *First-principles study of the ideal strength of Fe_3C cementite*, Mater. Sci. Eng., A 572 (2013), pp. 25–29.
[5] N. Garvik, P. Carrez, S. Garruchet, and P. Cordier, *Numerical modeling of the core structure of [1 0 0] dislocations in Fe_3C cementite*, Scr. Mater. 99 (2015), pp. 61–64.
[6] D. Grassi and M.W. Schmidt, *Melting of carbonated pelites at 8–13 GPa: Generating K-rich carbonatites for mantle metasomatism*, Contrib. Mineral. Petrol. 162 (2011), pp. 169–191.
[7] G.T. Herman, A.V. Lakshminarayanan, and A. Naparstek, *Convolution reconstruction techniques for divergent beams*, Comput. Biol. Med. 6 (1976), pp. 259–262.
[8] A. Inoue, T. Ogura, and T. Masumoto, *Dislocation structure of cementite in cold-rolled carbon steels*, J. Jpn. Inst. Met. 37 (1973), pp. 875–882.
[9] A. Inoue, T. Ogura, and T. Masumoto, *Deformation and fracture behaviours of cementite*, Trans. JIM 17 (1976), pp. 663–672.
[10] A. Inoue, T. Ogura, and T. Masumoto, *Microstructures of deformation and fracture of cementite in pearlitic carbon steels strained at various temperatures*, Metall. Trans. A 8 (1977a), pp. 1689–1695.
[11] A. Inoue, T. Ogura, and T. Masumoto, *Burgers vectors of dislocations in cementite crystal*, Scr. Metall. 11 (1977b), pp. 1–5.
[12] Y. Ishida, H. Ishida, K. Kohra, and H. Ichinose, *Determination of the Burgers vector of a dislocation by weak-beam imaging in a HVEM*, Philos. Mag. A 42 (1980), pp. 453–462.
[13] C. Jiang and S.G. Srinivasan, *Unexpected strain-stiffening in crystalline solids*, Nature 10 (2013), pp. 8–11.
[14] L.E. Kar'kina, T.A. Zubkova, and I.L. Yakovleva, *Dislocation structure of cementite in granular pearlite after cold plastic deformation*, Phys. Met. Metall. 114 (2013), pp. 234–241.
[15] A.S. Keh, *Imperfections and plastic deformation of cementite in steel*, Acta Metall. 11 (1963), pp. 1101–1103.
[16] W.-J. Kim, J. Wolfenstine, O.R. Ruano, G. Frommeyer, and O.D. Sherby, *Processing and superplastic properties of fine-grained iron carbide*, Metall. Trans. A23 (1992), pp. 527–535.
[17] A. Koréeda and K. Shimizu, *Dislocations in cementite*, Philos. Mag. 17 (1968), pp. 1083–1086.
[18] C. Messaoudi, T. Boudier, C.O. Sanchez Sorzano, and S. Marco, TomoJ (tomography software for three-dimensional reconstruction in transmission electron microscopy); (2007); software available at http://u759.curie.fr/fr/download/softwares/TomoJ.
[19] J.P. Morniroli, D. Vankieken, and L. Winter, *Electron diffraction. Dedicated software to kinematically simulate CBED patterns*, USTL, Lille, 1994.

[20] A. Mussi, P. Cordier, S. Demouchy, and C. Vanmansart, *Characterization of the glide planes of the [0 0 1] screw dislocations in olivine using electron tomography*, Phys. Chem. Miner. 41 (2014), pp. 537–545.
[21] A. Mussi, D. Eyidi, A. Shiryaev, and J. Rabier, *TEM observations of dislocations in plastically deformed diamond*, Phys. Status Solidi A 210 (2013), pp. 191–194.
[22] P. Penczek, M. Radermacher, and J. Frank, *Three-dimensional reconstruction of single particles embedded in ice*, Ultramicroscopy 40 (1992), pp. 33–53.
[23] E.F. Rauch and M. Véron, *Coupled microstructural observations and local texture measurements with an automated crystallographic orientation mapping tool attached to a TEM*, J. Mater. Sci. Eng. Tech. 36 (2005), pp. 552–556.
[24] E.F. Rauch, M. Véron, J. Portillo, D. Bultreys, Y. Maniette, and S. Nicolopoulos, *Automatic crystal orientation and phase mapping in TEM by precession diffraction*, Microsc. Anal. 22 (2008), pp. S5–S8.
[25] J.M. Rebled, L. Yedra, S. Estradé, J. Portillo, and F. Peiró, A new approach for 3D reconstruction from bright field TEM imaging: Beam precession assisted electron tomography, Ultramicroscopy 111 (2011), pp. 1504–1511.
[26] A. Rohrbach, S. Ghosh, M.W. Schmidt, C.H. Wijbrans, and S. Klemme, *The stability of Fe–Ni carbides in the Earth's mantle: Evidence for a low Fe–Ni–C melt fraction in the deep mantle*, Earth Planet. Sci. Lett. 388 (2014), pp. 211–221.
[27] J.G. Sevillano, *Room temperature plastic deformation of pearlitic cementite*, Mater. Sci. Eng. 21 (1975), pp. 221–225.
[28] M. Umemoto, Y. Todaka, and K. Tsuchiya, *Mechanical properties of cementite and fabrication of artificial pearlite*, Mater. Sci. Forum 426–432 (2003), pp. 859–864.
[29] R. Vincent and P.A. Midgley, *Double conical beam-rocking system for measurement of integrated electron diffraction intensities*, Ultramicroscopy 53 (1994), pp. 271–282.
[30] Y.D. Zhang, C. Esling, M. Calcagnotto, X. Zhao, and L. Zuo, *New insights into crystallographic correlations between ferrite and cementite in lamellar eutectoid structures, obtained by SEM–FEG/EBSD and an indirect two-trace method*, J. Appl. Crystallogr. 40 (2007), pp. 849–856.
[31] A.A. Zhukov and A.P. Ogarev, *The role of pressure in the formation of etch-resistant layers on rubbing surfaces of cast iron parts*, Sov. Mater. Sci.-Engl. Tr. 1 (1965), pp. 252–254.